

Data-driven Prediction of Ionic Conductivity in Solid-State Electrolytes with Machine Learning and Large Language Models

Haewon Kim^{1, #}, Taekgi Lee^{1, #}, Seongeun Hong¹, Kyeong-Ho Kim², and Yongchul G. Chung^{1,3,a)}

¹School of Chemical Engineering, Pusan National University, Busan, Korea (South) 46241

²Department of Materials Science and Engineering, Pukyong National University, Busan, 48513, Korea (South) 48513

³Graduate School of Data Science, Pusan National University, Busan, Korea (South) 46241

[#])These authors contributed equally.

^{a)}Author to whom correspondence should be addressed: drygchung@gmail.com

TOPICS: Machine learning, Large-language models, Solid-state batteries, Interatomic potentials

Abstract

Solid-state electrolytes (SSEs) are attractive for next-generation lithium-ion batteries due to improved safety and stability, but their low room-temperature ionic conductivity hinders practical application. Experimental synthesis and testing of new SSEs remain time-consuming and resource intensive. Machine learning (ML) offers an accelerated route for SSE discovery; however, composition-only models neglect structural factors important for ion transport, while graph neural networks (GNNs) are challenged by the scarcity of structure-labeled conductivity data and the prevalence of crystallographic disorder in CIFs. Here, we train two complementary predictors on the same room-temperature, structure-labeled dataset ($n = 499$). A gradient-boosted tree regressor (GBR) combining stoichiometric and geometric descriptors achieves best performance (MAE = 0.543 in $\log(\text{S}\cdot\text{cm}^{-1})$), and Shapley Additive exPlanations (SHAP) identifies probe-occupiable volume (POAV) and lattice parameters as key correlations for conductivity. In parallel, we fine-tune large language models (LLMs) using compact text prompts derived from CIF metadata (formula with optional symmetry and disorder tags), avoiding direct use of raw atomic coordinates. Notably, Llama-3.1-8B-Instruct achieves high accuracy (MAE = 0.657 in $\log(\text{S}\cdot\text{cm}^{-1})$) using formula and symmetry information, eliminating the need for numerical feature extraction from CIF files. Together, these results show that global geometric descriptors improve tree-based predictions and enable interpretable structure-property analysis, while LLMs provide a competitive low-preprocessing alternative for rapid SSE screening.

I. INTRODUCTION

Electrolytes are essential components of rechargeable batteries because they enable ionic transport between the cathode and anode and mediate charge transfer at the electrode-electrolyte interfaces. Solid-state electrolytes (SSEs) have emerged as critical components for next-generation batteries, offering improved thermal stability, nonvolatility, and greatly reduced flammability compared to conventional liquid electrolytes¹. Beyond these intrinsic safety advantages, SSEs also open the possibility of achieving higher energy densities by enabling the integration of Li-metal anodes and high-voltage cathodes, which are challenging to realize with liquid electrolytes². Achieving room-temperature ionic conductivities approaching those of liquid electrolyte ($\sim 10^{-3}$ - 10^{-2} S/cm) remains a central materials challenge for practical solid-state batteries³. A wide range of SSE chemistries have been explored in recent years, such as $\text{Li}_{10}\text{GeP}_2\text{S}_{12}$ (LGPS) and lithium argyrodites (e.g., $\text{Li}_6\text{PS}_5\text{X}$ where $\text{X} = \text{Cl}$, Br , I), and demonstrate high ionic conductivity, often exceeding 10^{-3} S/cm but they generally suffer from limited oxidative stability and interfacial reactivity⁴. In contrast, oxide-based SSEs, such as garnet-type (e.g., LLZO), NASICON-type (e.g., LATP) and perovskite-type (e.g., LLTO) offer comparatively wide voltage window and stability but often fall short in ionic conductivity (10^{-7} - 10^{-3} S/cm)⁵. Such relatively low ionic conductivity at room temperature remains a significant bottleneck to the widespread adoption of SSEs⁶.

Experimental synthesis and testing of solid-state electrolyte materials in search of the commercially viable ionic conductivity are both resource-intensive and time-consuming. To accelerate materials discovery, computational methods have recently been applied to estimate ionic transport properties in solid-state electrolytes. However, these computational approaches also present additional challenges. Classical molecular dynamics (MD) can estimate diffusion and conductivity (e.g., through mean-squared displacement combined with the Nernst-Einstein

relation or via Green-Kubo formalism⁷), but accuracy is highly dependent on the quality and transferability of the employed interatomic potentials, particularly their ability to reproduce migration barriers and defect energetics that govern ion transport^{8, 9}. Alternatively, ab-initio molecular dynamics (AIMD) based on density functional theory (DFT) can improve the description of ion motion by using a first-principles potential energy surface. However, the generation of AIMD trajectories across a large number of materials is computationally intensive, requiring considerable time and resources¹⁰. While the Nernst–Einstein relation is commonly used to estimate conductivity from diffusivities, it neglects correlation effects (collective ion motion) that can be significant in highly conducting SSEs¹¹. Additionally, AIMD simulations are performed at high temperatures to accelerate diffusion, and the room temperature ionic conductivity is estimated by extrapolating from these data. Such extrapolations can be unreliable for systems that exhibit non-linear Arrhenius behavior¹². To overcome the limited timescales accessible by AIMD, recent efforts have focused on developing and applying machine-learning interatomic potential (MLP) to generate trajectories on the nanosecond- to microsecond-scale. In selected systems, MLP-based MD simulations have shown encouraging agreement with experiment¹²⁻¹⁴.

Recent advances in machine learning (ML) and artificial intelligence (AI) have enabled direct prediction of ionic conductivity across wide composition space, provided that high-quality data sets are available. Hargreaves et al.¹⁵ released the Liverpool Ionics Data set (LiIon, 2023), which compiles experimentally reported 820 composition-conductivity data across 5-873 °C. Using this data set, they demonstrated composition-based machine learning (ML) screening, including attention-based architecture such as CrabNet¹⁶. Subsequent studies expanded these compilations and evaluated a variety of composition-based regression^{17,18,19}. Although ML algorithms have improved composition-based models, their performance remains constrained

by reliance on composition alone. Since ionic conductivity in solid-state electrolytes arises from ion hopping adjacent vacant sites, incorporating crystal structure information and defect/disorder-related descriptors (e.g., site occupancies and vacancy distributions) in training may further enhance predictive accuracy of the developed model.

Therrien et al.²⁰ recently introduced the Open Battery Electrolytes with Li: an eXperimental data set (OBELiX, 2025), which integrates both compositional and structural information to benchmark the role of structure in model training. OBELiX contains 599 experimentally measured room-temperature ionic conductivities with corresponding compositions, drawn from the LiIon data set and the Laskowski data set²¹. Of these, 321 crystal structures (CIFs) were obtained from the Inorganic Crystal Structure Database (ICSD), the Materials Project, and manual collection of data in the literature. The composition data were used to train conventional ML models (Random Forrest, Multi-Layer Perceptron), while CIF data were used to benchmark graph neural network (GNN) models. In their benchmark, composition-based models outperformed several crystal-graph neural network (GNN) models trained on the smaller CIF subset. They attributed this to two limitations of the structural data set: (i) the small-data regime and (ii) structural disorder in crystallographic data. Such disorder, arising from partially occupied or shared atomic sites that average multiple local configurations into a single structure, directly affects the local ionic environment^{22, 23}. In practice, partial occupancy and vacancy information are difficult to represent in structure-only graph encoding, and in small-data regimes these factors can degrade model performance. These observations motivate the exploration of alternative ML architecture that can jointly encode compositional and structural information in representations more amenable to learning complex structure-property relationships.

As an alternative approach to incorporate structural information as features, recent studies have explored the use of large language models (LLMs) to process materials data in interpretable textual forms. LLMs can capture detailed structural features of crystalline materials, including disorder-related information, through textual representations. LLMs have been applied widely to predict properties of diverse systems, including zeolites²⁴, MOFs²⁵, transition metal complexes²⁶, drugs²⁷, alloys^{28, 29} and polymers³⁰. Notably, Rubungo et al.³¹ demonstrated that LLMs can predict crystalline materials properties by fine-tuning on text-based descriptions derived from CIFs using tools such as Robocrystallographer³².

These developments suggest that combining structural descriptors with modern ML architecture could overcome the limitations of composition-only models. However, the scarcity of experimentally determined structures for many SSE compositions remains a barrier. In this work, we develop two complementary data-driven predictors for room-temperature ionic conductivity that differ only in how crystal structures are represented. First, we curate a structure-labeled dataset of 499 inorganic SSEs by combining experimentally reported CIFs (OBELiX) with 152 additional USPEX-generated structures relaxed using CHGNet, plus a small set of DFT-optimized structures from MP/OQMD. Next, we train a gradient-boosted tree regressor (GBR) on engineered stoichiometric and geometric descriptors and interpret the learned structure-property relationships using SHAP to identify which global features (e.g., lattice scale and accessible volume) most strongly correlate with conductivity. In parallel, we fine-tune multiple large language models (LLMs) using compact text prompts constructed from CIF metadata (formula and selected crystallographic metadata, when available) to evaluate whether competitive accuracy can be obtained without direct parsing of raw CIF coordinates. Because both approaches are trained and evaluated on the same data split and target definition,

the results provide a controlled comparison between numerical feature engineering and text-based learning for SSE screening.

II. Methods

A. Dataset Curation

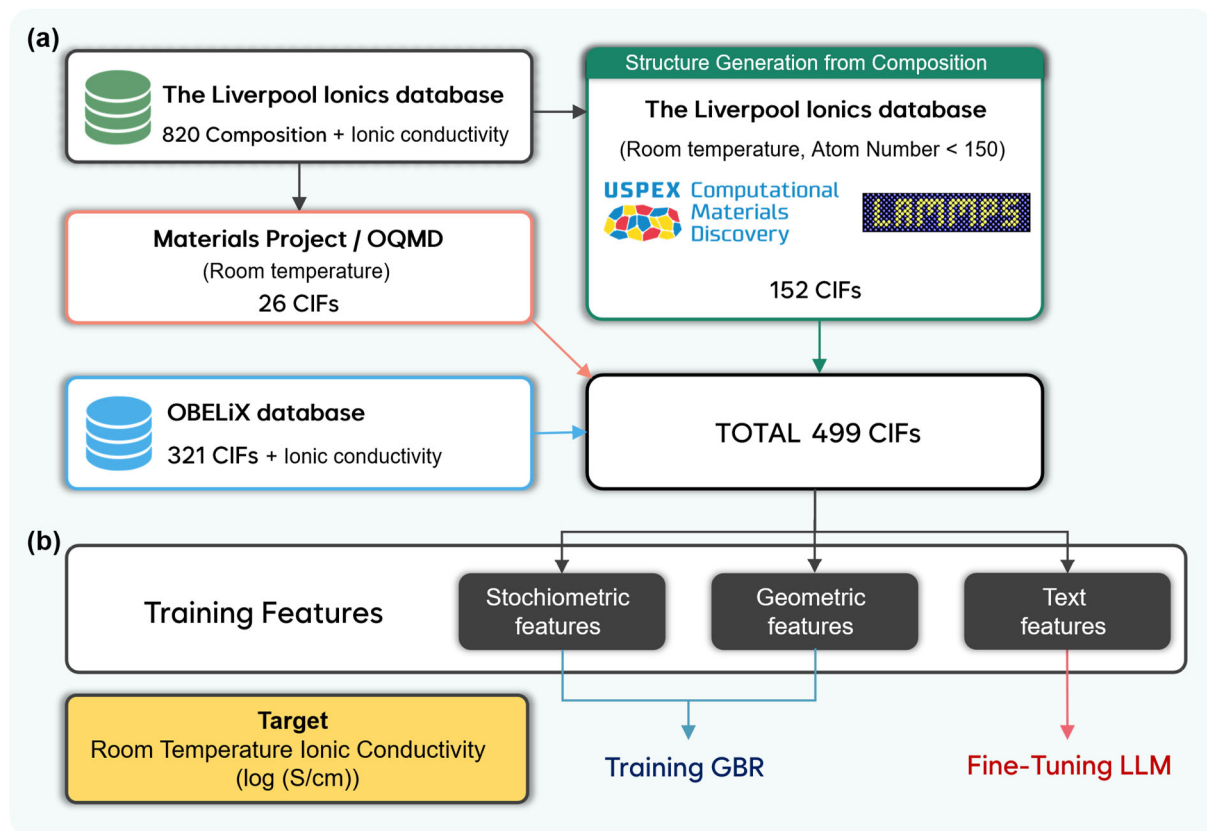


Figure 1. (a) Data curation and (b) model training part of overall workflow.

The overall dataset curation and model training workflow of this study is summarized in **Figure 1**. The dataset was constructed by combining composition data collected from the LiIon database with CIF structures from the OBELiX dataset and our generated dataset. In addition, DFT optimized structure files were collected from the materials project (MP) and the open quantum materials database (OQMD) based on the LiIon database. In this process, structures with stoichiometric errors resulting in improper charge balance in the original dataset were excluded. The schematic of the dataset construction is shown in **Figure 1(a)**. Based on this

dataset, features were generated, and predictive models were trained as shown in **Figure 1(b)**.

Details of each step are discussed in the following sections.

B. Structure Generation and Validation

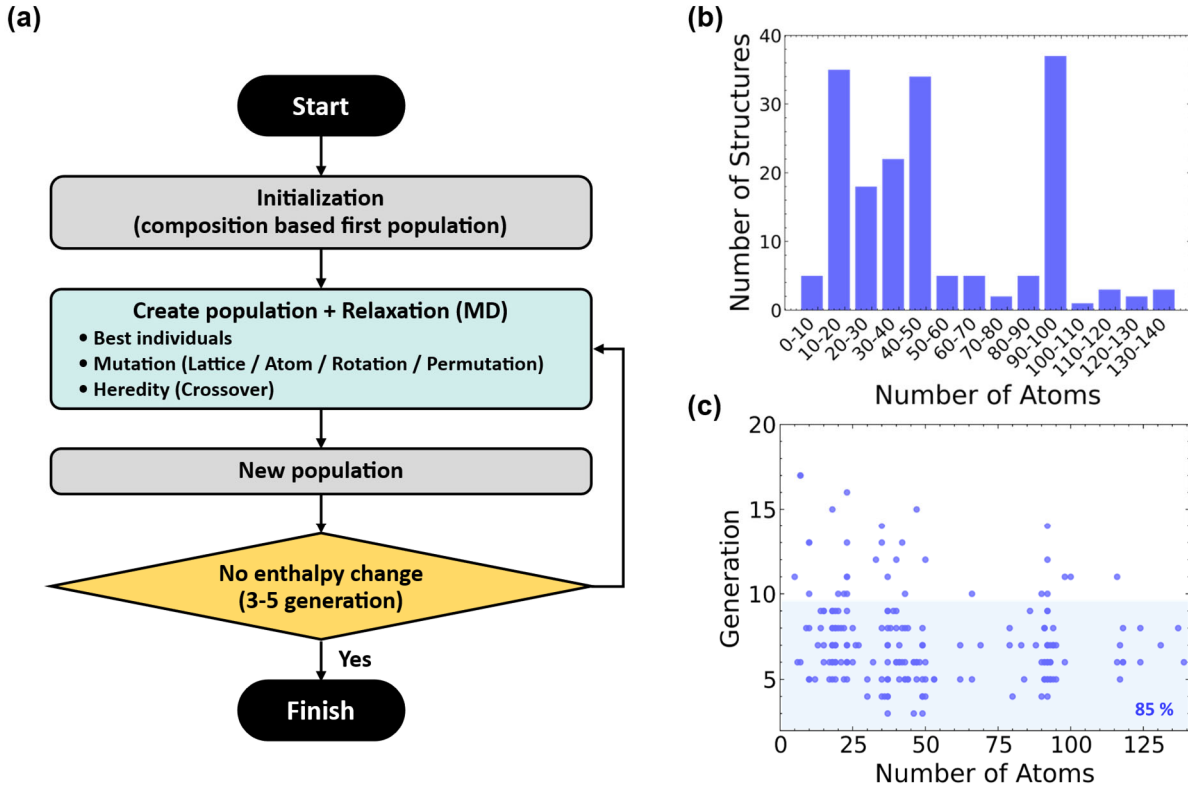


Figure 2. (a) Workflow of structure generation in USPEX based on a genetic algorithm. (b) Distribution of atom numbers in the generated structures (c) Number of generations as a function of atom numbers.

We employed the USPEX (Universal Structure Predictor: Evolutionary Xtallography)³³⁻³⁵ software to generate crystal structures from composition data of LiIon database. The overall structure generation algorithm of USPEX is shown in **Figure 2(a)**. USPEX generates structures by constructing a random initial population from the stoichiometric formula, followed by energy minimization. In genetic algorithm-based structure generation, thermodynamically stable structures are identified through iterative optimization involving heredity, mutation, and permutation. For variation operators in USPEX, atom mutation involves slight displacements of atomic positions, while permutation swaps the chemical identities of randomly chosen atom pairs. Heredity operator combines spatially coherent slabs from two parent structures, with

their lattice vector matrices serving as weighted averages³⁶. Although computationally intensive, these generation methods reduce the risk of trapping in local minima of the potential energy surface. At each generation, enthalpies of the candidate structures are calculated after energy minimization, and the structures with the lowest enthalpy values are selected to generate the next population. To increase computational efficiency of the search, we replaced density functional theory (DFT) calculation of enthalpy evaluation with all-atom machine learning potential (MLP)-based molecular dynamics (MD) simulations. To initiate the generation process, all chemical formulas were reduced to their simplest integer stoichiometric form, and the number of atoms per structure was restricted to fewer than 150 to ensure computational feasibility. **Figure 2(b)** shows the distribution of atom counts in the structures generated from reduced compositions. In each generation, structural relaxation was carried out until the enthalpy values converged within the same range over 3–5 successive generations. Approximately 85% of the structures achieved enthalpy convergence before the 10th generation. Number of generations as a function of atom numbers are shown in **Figure 2(c)**.

MD simulations were carried out using the LAMMPS (2 Aug 2023 release)³⁷ using periodic boundaries in all directions. CHGNET³⁸ model is a machine-learned interatomic potential trained on energies, forces, stresses, and magnetic moments from the Materials Project trajectory data set. CHGNET has been shown to perform reliably even for systems containing transition metals³⁹. Benchmarking studies have also demonstrated that CHGNet reproduces AIMD results with near-DFT accuracy across a broad range of lithium-ion solid electrolytes³⁸. In particular, CHGNet accurately captures highly nonlinear diffusion phenomena such as the sharp reduction in activation energy and the emergence of activated Li diffusion networks in garnet-type materials in excellent agreement with DFT benchmarks. These results indicate that CHGNet reliably models the strong local Li-Li interactions and complex diffusion environments characteristic of solid-state ionic conductors. We used CHGNET-LAMMPS-

0.3.0 pair coefficient to evaluate energies and forces of generated structures. Both atomic and cell relaxation, the Nose-Hoover thermostat and barostat are used as implemented in the LAMMPS. The system was equilibrated by NPT ensemble at 50 K and 1000 bar, with thermostat and barostat damping constants of 1 ps. The neighbor list was updated every step with a cutoff distance of 8 Å. Each simulation was run for 1,000 steps with 1 fs timestep (total of 1 ps) for integrating Newton’s equation of motions. Properties(E_{pot} , E_{kin} , E_{tot} , T , p , V) are recorded every step and atomic configurations saved every 50 steps for subsequent analysis. In total, 152 structures were generated using USPEX method and the final MD relaxations using MLP model were conducted under the same conditions (NPT ensemble; 50 K and 1000 bar) as the enthalpy relaxation for an additional 20 ps simulation for all structures.

C. Feature Extraction and Models

To develop ML model, we extracted features from CIFs obtained from the snapshot at the end of 20 ps relaxation simulations and the original CIFs from the OBELiX, Materials Project (MP), and Open Quantum Materials Database (OQMD). The ionic conductivity data corresponding to the structures were collected from the LiIon and OBELiX datasets. Stoichiometric features were employed to reflect the compositional properties of the structures, and geometric features from CIFs were generated to capture the structural characteristics of the SSEs. In the case of LLMs, text-based properties that integrate both stoichiometric and geometric features are required. Therefore, text-based structural information from CIF files was utilized for LLM fine-tuning. All types of features used for model training are presented in **Figure 3**.

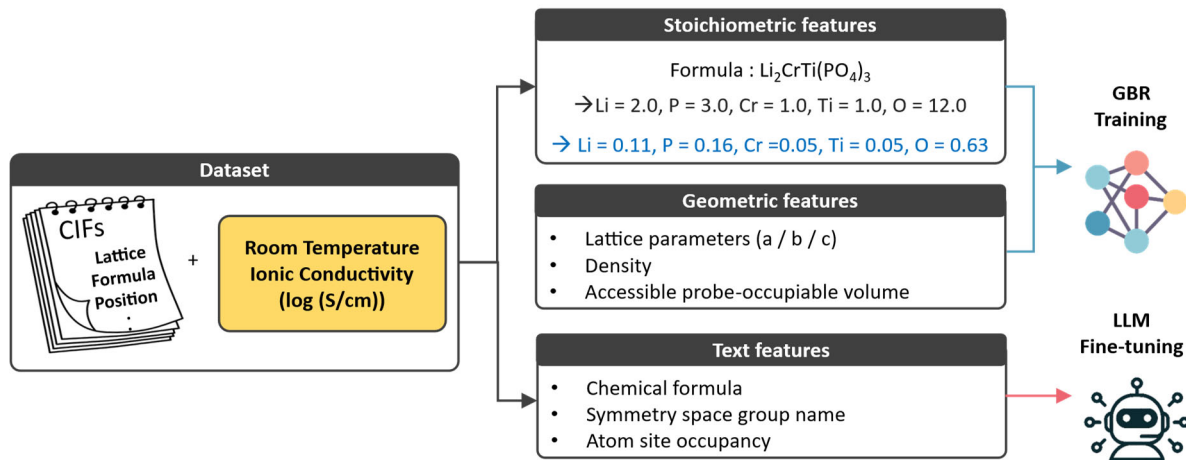


Figure 3. Features generated for model training. Features are extracted from the collected CIFs and Stoichiometric, geometric and text-based features were generated for training models.

Gradient Boosting Regression (GBR) Training

For the regression model, we employed the XGBOOST GBR algorithm to develop a predictive model for experimental ionic conductivity. For the stoichiometric features, the compositions were obtained using the `chemparse`⁴⁰ Python package. The elemental ratios contained in each composition used as stoichiometric features. Geometric features are generated from original CIFs. Lattice parameters (a/b/c) were directly obtained from the CIF files, and vacancy volume-related descriptors were computed based on the analysis of the Voronoi network, implemented in the `Zeo++3.0` software⁴¹⁻⁴³. Ion transport mechanism for solid electrolytes usually involves the movement of ions originating from a stable site via high energy transition state to another stable site⁴⁴⁻⁴⁶. The movement of ions is expected to be affected by lattice density and the porosity, which were regarded as key factors in ionic conductivity⁴⁷. Accordingly, we used density (g/cm³), gravimetric accessible probe-occupiable volume (POAV, cm³/g), and lattice parameters from CIF files as the geometric features. All features were processed through an integrated code to produce .csv files from CIFs.

Prior to training, we standardized all input features using z-score normalization implemented with StandardScaler in scikit-learn⁴⁸ (removing the mean and scaling to unit variance). The dataset was divided into training (399 data points) and test (100 data points) set with an 8:2 ratio using a diversity selection method. By this method, the training dataset was constructed by sampling from the entire dataset that the ionic conductivity distribution was preserved. During training, 6-fold cross validation was implemented using the scikit-learn⁴⁸ library and the hyperparameter tuning was performed using the scikit-optimize library. Hyperparameters were tuned using Bayesian optimization, with the goal of minimizing the mean squared error (MSE) of the model. Optimized parameters are summarized in **Table 1**.

Table 1. Parameters of GBR models for ionic conductivity prediction.

Model	Parameters	Values
Gradient Boosting Regression (GBR)	n_estimators	242
	reg_lambda	24.922
	reg_alpha	2.345
	max_depth	8
	num_parallel_tree	8
	min_child_weight	1
	subsample	0.659
	learning_rate	0.084
	gamma	0.015

We used the coefficient of determination (R^2), spearman's rank correlation coefficient (SRCC), root mean squared error (RMSE), and the mean absolute error (MAE) to quantify the performance of developed model.

$$R^2 = 1 - \frac{\sum_{i=1}^n (y - \hat{y})^2}{\sum_{i=1}^n (y - \bar{y})^2} \quad (1)$$

$$SRCC = 1 - \frac{6 \sum d_i^2}{n(n^2 - 1)} \quad (2)$$

$$MAE = \frac{\sum_{i=1}^n |y - \hat{y}|}{n} \quad (3)$$

$$RMSE = \sqrt{\frac{\sum_{i=1}^n (y - \hat{y})^2}{n}} \quad (4)$$

where y , \hat{y} , and \bar{y} denote the true value, predicted value, and the mean of the true values; d_i is the difference in ranks given to the two variables values for each item of the data; n is the number of data points. To explain the importance of each feature, we calculate the SHAP value to analyze the model.

LLM Fine-tuning

We fine-tuned three large language models, Llama-3.1-8B-Instruct, Mistral-7B-Instruct-v0.3, and Qwen3-8B, to predict ionic conductivity, using the same training dataset as employed for the GBR model. Fine-tuning improves a general-purpose LLM by training the model on a specific dataset. This helps the model develop a deeper understanding of a particular task, allowing it to produce more relevant responses to queries⁴⁹. Hugging Face Transformers⁵⁰ are used to load the pretrained models and employed Unslloth⁵¹ which makes fine-tuning process more efficient even with limited computational resources. Low-rank adaptation (LoRA)⁵² was applied to the process, which significantly reduces the number of trainable parameters and GPU memory requirements. An identical fine-tuning hyper parameters were applied to all three models (**Table 2**). The training was conducted using an NVIDIA GeForce RTX 4090 GPU. The batch size per device was set to 4, and the gradient accumulation steps were set to 2 before each backward/update pass. Under these settings, the model training required approximately 10 minutes to complete for 15 epochs.

Table 2. Parameters of LLM models for ionic conductivity prediction model.

Type	Parameters	Values
Training	Alpha	64
	Dropout	0.05
	Target modules	q_proj, k_proj, v_proj, o_proj, gate_proj, up_proj, down_proj
	Optimizer	Adam 8bit
	Learning Rate	2×10^{-4}
	Weight Decay	0.01
Inference	Scheduler	Cosine
	Epochs	15
	Max new tokens	12
Inference	Do sample	True
	Temperature	0.7
	Top k	10

Table 3. LLM prompt format.

LLM Prompt		
System prompt	You are a domain expert in materials science specializing in ionic transport. Your task is to predict the logarithm (base-10) of the ionic conductivity of a solid electrolyte. You will be given the material's chemical formula and property description. Output ONLY a single numeric value (the predicted $\log_{10}(\text{conductivity})$) on one line. Do not print units, JSON, labels, extra spaces, or any additional text. Be as precise as possible (use sufficient decimal places)	
	Case 1 formula: value	Case 2 <formula: value> <symmetry: value>
Input prompt	Case 3 <formula: value> <disorder: value>	Case 4 <formula: value> <symmetry: value> <disorder: value>
Output prompt	value	

The prompt templates employed for training utilized a zero-shot strategy, as summarized in **Table 3**⁵³. Processing solid-state electrolyte (SSE) crystallographic data leads to a complication because of the presence of disorder (i.e., partial occupancy) in the structure files, which is introduced to model the various elemental site-occupancies⁵⁴. Since the standard tool to convert CIFs to text, Robocrystallographer³², cannot parse CIFs containing such disorder, the chemical

formula, symmetry space group name, and atom site occupancy were obtained directly from the CIF files to construct the input prompts. Also, direct use of raw CIF files as text input was avoided because long floating-point atomic coordinates are tokenized into fragmented digit-level subunits, preventing the LLM from interpreting geometric information and introducing substantial numerical noise. Curated structural descriptions preserve essential structural features in efficient manner, leading to more stable fine-tuning.

Four distinct cases were designed for these inputs: Case 1 included only the chemical formula, and this is baseline feature for all subsequent cases; Case 2 incorporated the symmetry group; Case 3 added a disorder classification. This classification was categorized in four classes – “Li cation disorder”, “Other atom disorder,” “Li cation and Other atom disorder,” and “No disorder” – specifically to differentiate between disorder in the Li-ion sites and other atoms, given that higher levels of Li-vacancy disorder are known to significantly increase Li-ion conductivity⁵⁵. Finally, Case 4 combined all available information including the chemical formula, symmetry group, and disorder classification.

The output prompt required the LLM to predict the logarithm of the ionic conductivity (without unit). An illustrative example of the LLM input text is provided in **Table 4**. The chemical formula and space group were obtained from the CIF file. Based on the partial atomic occupancies of 0.86 and 0.62 for Li and 0.57 and 0.46 for Y, the disorder was described as exhibiting ‘Li cation and Other atom disorder’.

Table 4. Example LLM input text from cif file

CIF File	LLMs Input	
Chemical Formula	Li3YCl6	
Symmetry group	P-3m1	
Atom site occupancy (X, Y, Z, Partial Occupancy (P.O))		
Li0	X: 0.00 Z: 0.50	Y: 0.33 P.O: 0.86 Case 1) formula: Li3YCl6
Li1	X: 0.00 Z: 0.00	Y: 0.33 P.O: 0.62 Case 2) <formula: Li3YCl6> <symmetry: P-3m1>
Y2	X: 0.33 Z: 0.49	Y: 0.67 P.O: 0.57
Y3	X: 0.33 Z: 0.98	Y: 0.67 P.O: 0.43 Case 3) <formula: Li3YCl6> <disorder: Li cation and Other atom disorder >
Y4	X: 0.00 Z: 0.00	Y: 0.00 P.O: 1.0 Case 4)
Cl5	X: 0.11 Z: 0.78	Y: 0.22 P.O: 1.0 <formula: Li3YCl6> <symmetry: P-3m1> <disorder: Li cation and Other atom disorder >
Cl6	X: 0.13 Z: 0.75	Y: 0.56 P.O: 1.0
Cl7	X: 0.21 Z: 0.28	Y: 0.42 P.O: 1.0

III. Results

A. Dataset Composition and Label Distribution (room-temperature dataset)

We first summarize the composition, family coverage, and label distribution of the room-temperature dataset used for model training and evaluation. Because conductivity spans many orders of magnitude, all models are trained and evaluated on $\log_{10}(\sigma/(\text{S}\cdot\text{cm}^{-1}))$. The final dataset contains 499 labeled crystal structures measured near room temperature (20 – 34 °C, median 27 °C), comprising 321 OBELiX structures, 152 USPEX-generated structures that passed feature extraction, and 26 MP/OQMD structures. Families include NASICON (~20%), garnets (~15%), thiophosphates (~20%), reflecting diversity in the curated SSE dataset but with some biases toward dense oxides/sulfides. The target property $\log_{10}(\sigma/\text{S cm}^{-1})$ spans –17.38 to –1.60, covering 16 orders of magnitude in ionic conductivity. Using σ thresholds of 10^{-6} , 10^{-4} , and 10^{-3} S/cm, the dataset includes 186 low-, 146 moderate-, 103 high-, and 64 superionic-conductivity materials. **Figure 4(a)** illustrates a heat map of elemental occurrence across the dataset. All structures contain Li atom, while oxygen atom is present in 349 structures, reflecting the dominance of oxide-type electrolytes in the dataset. Other frequently observed elements include P, S, La, and Ti. **Figure 4(b)** shows the distribution of structures as a function of ionic conductivity. The ionic conductivity range was divided into four categories: low ($< 10^{-6}$ S/cm), moderate ($10^{-6} < \sigma < 10^{-4}$ S/cm), high ($10^{-4} < \sigma < 10^{-3}$ S/cm)⁵⁶, and superionic ($> 10^{-3}$ S/cm)⁵⁷, the latter being competitive with liquid electrolytes. Because the ionic conductivities in our dataset are distributed over several orders of magnitude, we use $\log(\text{S}/\text{cm})$ as the target property rather than the raw conductivity σ . Directly training on σ (S/cm) leads to an inherent imbalance in the loss function, such as structures with high conductivity dominate the error.

Distribution of training sets from the diversity selection is shown in **Figure 4(d)**. In addition, among the 321 CIF structures in OBELiX dataset, 248 show partial occupancies, as

summarized in **Figure 4(c)**. In our workflow, all structures were explicitly labeled as disordered (i.e., containing partial occupancies, $PO \neq 1$) or non-disordered ($PO=1$), and this information was incorporated as a feature for training GBR model and also fine-tuning the LLM models.

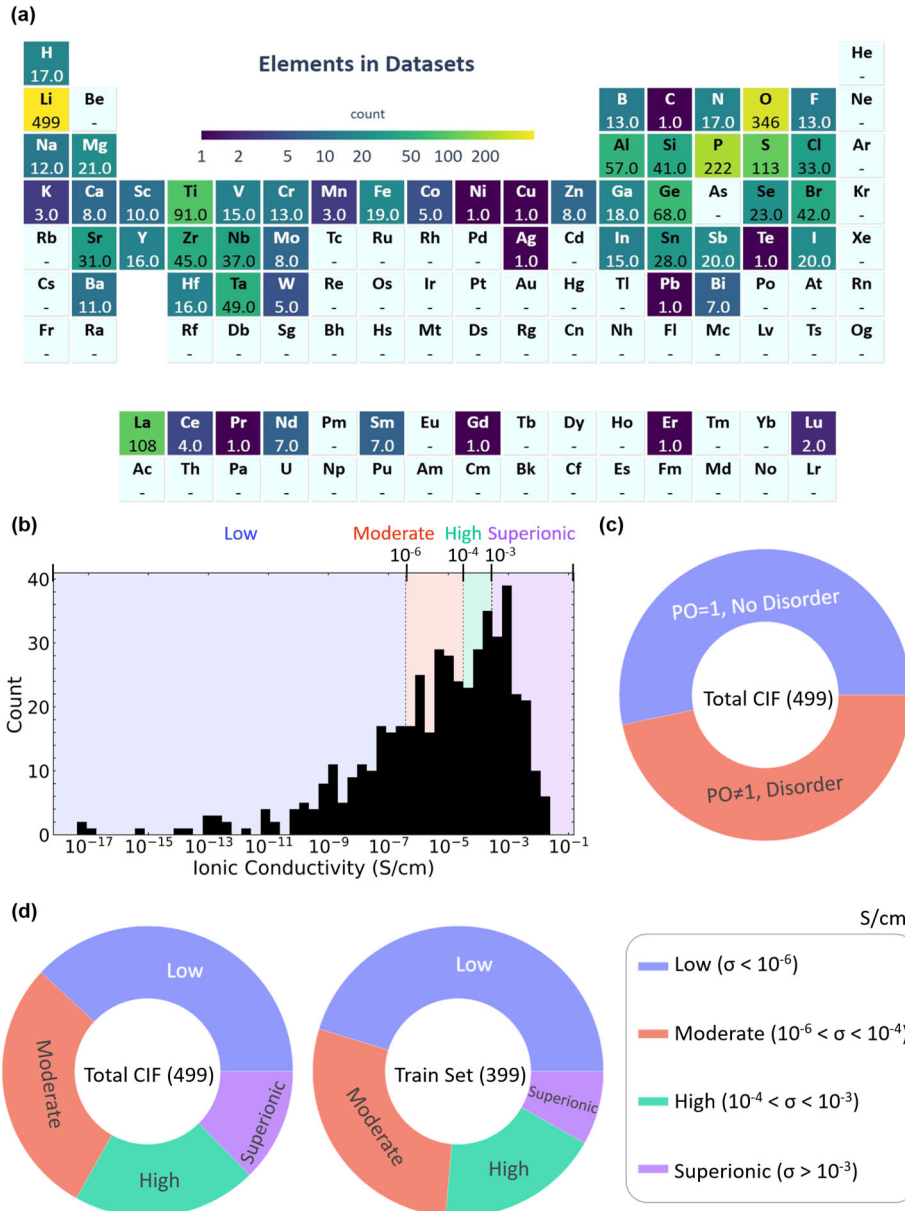


Figure 4. (a) The distribution of elements contained in dataset are shown on the periodic table, generated using pymatviz⁵⁸. (b) Distribution of CIF structures across ionic conductivity ranges, categorized as low ($<10^{-6}$ S/cm), moderate (10^{-6} - 10^{-4} S/cm), high (10^{-4} - 10^{-3} S/cm), and superionic ($>10^{-3}$ S/cm); (c) Proportion of structures with partial occupancies among the entire set of CIF files. (d) Ionic conductivity distribution of the dataset used for model training compared with entire dataset.

The dataset collected in this study consists exclusively of inorganic electrolytes. The top 6 families of solid-state electrolytes represented in the overall dataset are summarized in **Table 5**. Full dataset are primarily composed of oxide families (garnet, NASICON, perovskite) and sulfide families (LGPS, argyrodite). Overall, the room-temperature dataset spans many orders of magnitude in conductivity and is dominated by oxide and sulfide chemistries, while also containing a high fraction of partially occupied (i.e., disordered) CIFs. This motivates our two-track modeling strategy: GBR tests whether global geometric descriptors help beyond composition while LLM prompts explicitly encode disorder/symmetry metadata that standard CIF-to-text tools struggle to capture.

Table 5. Top six solid-state electrolyte families represented in the overall dataset.

Rank	Family	Ratio
1	Li-NASICON (Oxide)	0.21
2	Garnet (Oxide)	0.15
3	Perovskite (Oxide)	0.12
4	Argyrodite (Sulfide)	0.12
5	LISICON (Oxide)	0.08
6	Thio-LISICON (Sulfide)	0.05

B. USPEX+CHGNet Structure Generation and Validation

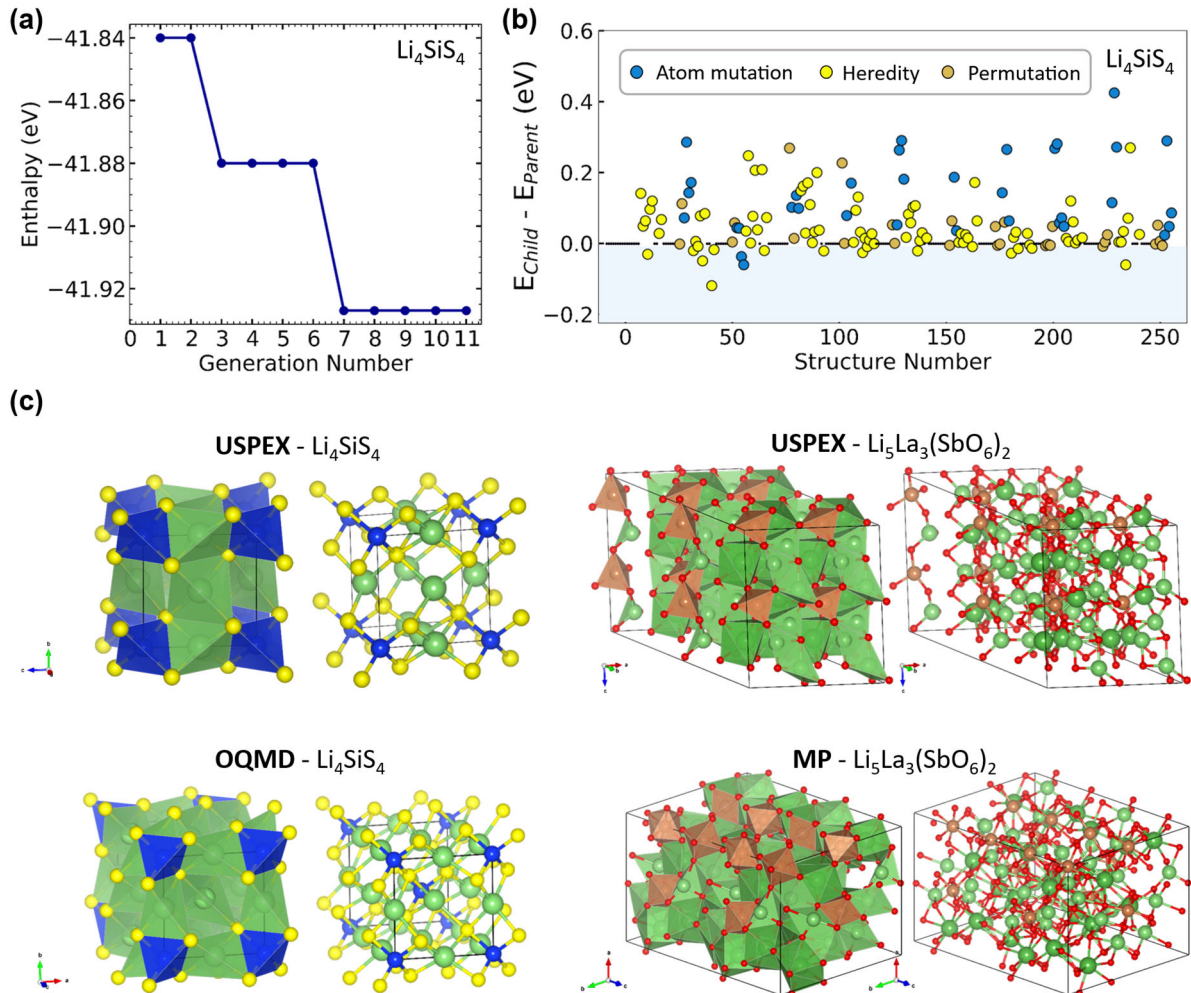


Figure 5. (a) Enthalpy change of Li_4SiS_4 across generations. (b) Enthalpy variation ($E_{\text{child}} - E_{\text{parent}}$) during structural mutation. (c) Structures generated from compositions with USPEX compared with structures collected from MP and OQMD.

Figure 5 shows the structure generation results using USPEX. As shown in **Figure 5(a)**, for the representative sample structure (Li_4SiS_4), the enthalpy generally decreased stepwise with the progress of 11 generation cycles. **Figure 5(b)** displays the entire population of structures generated during this process as a function of enthalpy difference between the child and parent structures ($E_{\text{child}} - E_{\text{parent}}$) for each variation. Points with a value below 0.0 indicate a successful reduction in enthalpy. Among 3 types of genetic operations (atom mutation, heredity, permutation) at each generation, the heredity operation (both parent structures are cut into two pieces and recombined) leads to enthalpy reductions. The representative sample structures

(Li_4SiS_4 and $\text{Li}_5\text{La}_3(\text{SbO}_6)_2$) obtained from USPEX were further compared with those reported in the literature, as shown in **Figure 5(c)**. To quantitatively assess the similarity between the USPEX-generated structures and reference geometries from the Materials Project and OQMD, we constructed supercells for each structure pair and compared their lattice parameters as well as atomic arrangements (**Table 6**). The supercell lattice lengths showed close agreement across examined cases, indicating that the global geometric scale of generated structures is consistent with MP/OQMD structures. We further computed the root-mean-square displacement (RMSD) of atomic positions using the StructureMatcher module in pymatgen. For Li_4SiS_4 , the calculated RMSD was 0.320 Å, while for $\text{Li}_5\text{La}_3(\text{SbO}_6)_2$, the RMSD was 0.521 Å. These RMSD values (0.320 – 0.521 Å) represent approximately 12 – 20% of typical Li-S bond lengths (~2.4 – 2.6 Å), confirming that positional deviations remain within chemically reasonable limits.

Table 6. Structural similarity between USPEX-generated structure and MP/OQMD-collected structures.

	Li_4SiS_4 (USPEX)	Li_4SiS_4 (OQMD)	$\text{Li}_5\text{La}_3(\text{SbO}_6)_2$ (USPEX)	$\text{Li}_5\text{La}_3(\text{SbO}_6)_2$ (MP)
Supercell atom #	18	18	88	88
_cell_length_a	11.156	11.587	11.976	11.199
_cell_length_b	11.156	11.587	10.332	11.213
_cell_length_c	11.158	10.376	11.976	11.218
RMSD (Å)	0.320		0.521	

When visualizing Li_4SiS_4 structure collected from the OQMD, we observe similarity in the atomic arrangements. Li atoms form tetrahedrons with four neighboring S atoms, and Si atoms also form tetrahedrons with four neighboring S atoms. However, structures where S atoms form hexahedrons are not present in the USPEX-generated structures. Similarly, for $\text{Li}_5\text{La}_3(\text{SbO}_6)_2$, the Li atoms forming octahedrons with six neighboring O atoms are consistent with structure from MP. However, the Sb atoms, which form octahedrons in the MP structure, appeared as hexahedron in the USPEX-generated structure. Despite these differences, the polyhedron

structures of Li atoms in both USPEX-generated sample structures are identical to those in the DFT optimized structures. While some atoms exhibited different polyhedron structures, the elements of the adjacent atoms are consistent between both structures, indicating a structural similarity with optimized structures and those from MP and OQMD database.

To assess the physical plausibility of the 152 crystal structures generated by USPEX and subsequently relaxed using CHGNet, we performed validation using automated analysis tools implemented in pymatgen. We evaluated the minimum interatomic distances across all structures to identify any unphysically short bonds that would indicate structural instability or unrealistic atomic configurations. Except for one structure, all minimum bond lengths exceeded 1.3 Å, which falls within expected chemically reasonable ranges for the elements considered. . The single outlier featured an O-H bond of 0.96 Å, which is consistent with experimental hydroxyl bond lengths (~0.97 Å), confirming it is physically valid. Furthermore, to assess whether the USPEX-predicted structures correspond to stable crystal phases, each optimized structure was further equilibrated for an additional 20 ps NPT MD simulation at 300 K and 1 atm using CHGNet. **Figure 6** shows the potential energy of all 152 structures during the MD trajectory. Throughout the simulations, no atom loss or structural collapse was observed. These results suggest that the generated structures maintain structural integrity under experimentally measured conditions on the timescale of the simulation.

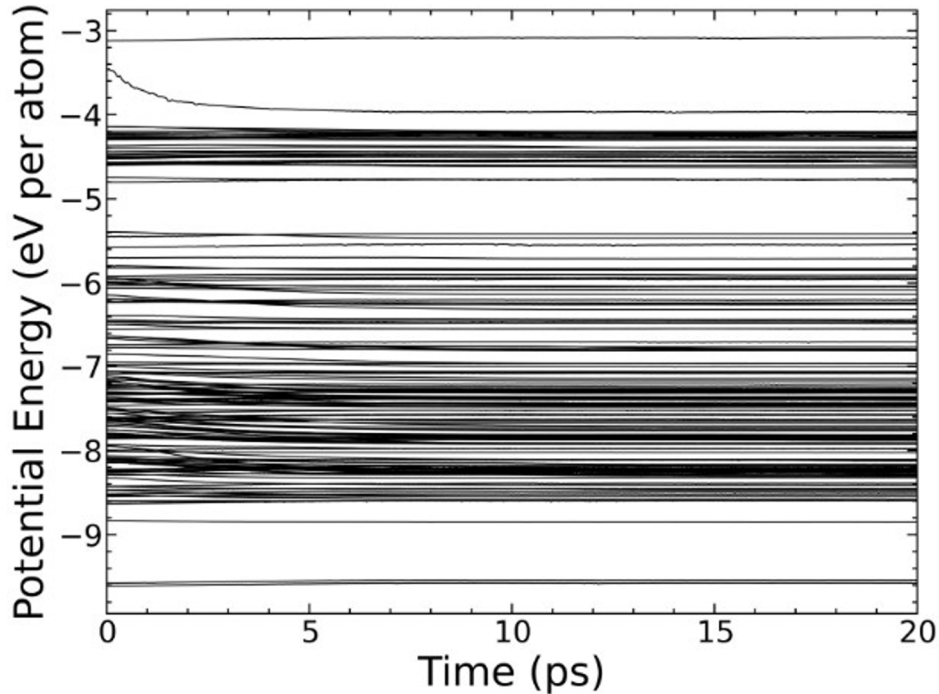


Figure 6. Energy relaxation results (energy per atom) of 152 USPEX-generated structures obtained from 20 ps NPT-MD using CHGNet at 300 K and 1 atm.

These validations indicate that the USPEX with CHGNet workflow produces physically plausible geometries that are broadly consistent with reference database structures and remain stable during short finite-temperature MD. The resulting generated structures expand structural coverage for compositions lacking experimentally resolved CIFs, enabling structure-aware model training at room temperature.

C. Gradient-boosted Trees: Effect of Compositional versus Geometric Descriptors and SHAP Interpretation

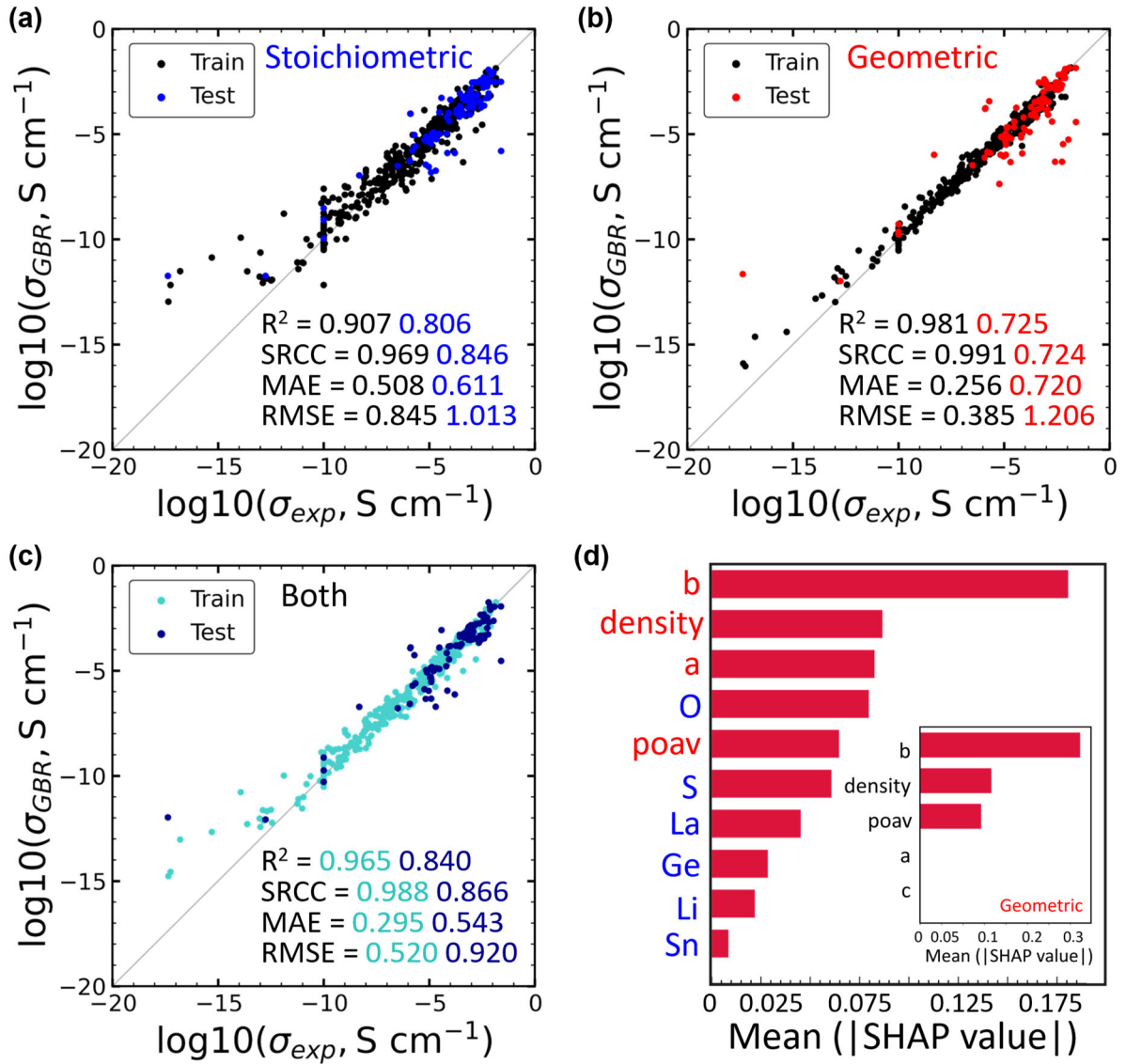


Figure 7. (a) Stoichiometric features only. (b) Geometric features only. (c) All features. (d) SHAP analysis of feature importance using all features and geometric features.

The performance of the Gradient Boosting Regressor (GBR) model was evaluated using stoichiometric features, geometric features, and a combination of both. **Figures 7(a)-(c)** visualizes the predictive performance of the GBR model when using the stoichiometric, geometric, and combined features, respectively. **Figure 7(d)** presents the results of a feature importance analysis for the model trained with combined features, quantified by SHAP values. When trained solely on stoichiometric features, the model achieved a test MAE of 0.611. However, the R^2 value of 0.907 on the training set indicated insufficient training convergence

compared to other models. When trained only on geometric features, a model achieved a test MAE was 0.720 log(S/cm). The test RMSE value was 1.206 log(S/cm), indicating a high frequency of data points with large error values.

For the test SRCC, the model achieved a value of 0.846 when using only stoichiometric features, indicating strong ranking performance. In contrast, when trained solely on geometric features, the SRCC decreased to 0.724, representing the lowest performance. The best performance was obtained when both feature types were combined. In this case, the model achieved a test R^2 of 0.840, a test SRCC of 0.866, a Test MAE of 0.543, and the lowest RMSE of 0.920. These results indicate that the predictive accuracy of stoichiometric features can be significantly enhanced when the geometric characteristics of the solid electrolytes are also incorporated. Notably, although the training set contained relatively few data points in the superionic conductivity range, the model showed strong predictive performance in the superionic regime of the test set.

According to the SHAP analysis, the **lattice parameter b** was identified as the most influential feature in the combined model. This was followed by **density (g/cm³)**, **lattice parameter a**, the **stoichiometric ratio of oxygen (O)**, and the **gravimetric probe-occupiable accessible volume (POAV)**. Among the geometric descriptors, the lattice parameter b showed the strongest impact on ionic conductivity prediction. As one of the three fundamental descriptors (a, b, c) representing the size of the unit cell, the lattice parameters are sensitive to changes in composition and stoichiometry. Variations such as elemental doping, the introduction of defects, or the presence of vacancies can directly alter unit cell dimensions⁵⁹. We found that SSEs with similar chemical compositions and closely related stoichiometries in dataset tend to cluster around comparable ionic conductivities and share nearly identical b-axis lattice parameters. This suggests the model is leveraging lattice anisotropy to distinguish material families. Unlike

cubic systems, approximately 69% of solid electrolytes in our dataset exhibit structural anisotropy ($a \neq b \neq c$). This suggests the model uses lattice parameter b as a statistical proxy to distinguish between high-performance material families, rather than identifying a universal diffusion axis. Even when the model was trained using only geometric features (**Figure 7d inset**), the lattice parameter b remained the dominant descriptor, confirming that it serves as a critical structural fingerprint independent of explicit compositional inputs. In high-symmetry anisotropic structures such as orthorhombic β -Li₃PS₄, crystallographic conventions align the b-axis with preferred Li-ion diffusion pathways, as demonstrated by MD studies⁶⁰. However, a significant portion of our dataset (~39%) consists of structures with P1 space group symmetry, where axis labels are assigned by convention rather than crystallographic symmetry. Therefore, the importance of 'b' in our model reflects both physical anisotropy in high-symmetry systems and its effectiveness as a statistical descriptor that correlates with high-performance material families.

The most important stoichiometric feature was ratio of oxygen. In the dataset, approximately 60% of the electrolytes are oxides, where oxygen plays a dual role: it stabilizes the lattice due to its high electronegativity but also forms strong electrostatic interactions with Li⁺, narrowing the conduction bottlenecks⁶¹. Consequently, doping anion sites with oxygen, which modifies the oxygen ratio, can affect ion migration pathways. This explains the strong importance of oxygen ratio observed in the feature influence analysis. Finally, the gravimetric accessible probe-occupiable volume (POAV, cm³/g) was identified as another key structural descriptor. POAV represents the available free volume within the lattice, which is directly linked to the ease of Li⁺ migration. Larger accessible volumes and vacancy channels are known to reduce migration barriers, thereby enhancing conductivity⁴⁷. These SHAP results show the geometric descriptors improve predictive accuracy relative to composition alone, indicating that global

structural fingerprints capture transport-relevant information even without explicit diffusion-path calculations. The SHAP ranking should be interpreted as correlation within this dataset, motivating future work using axis-invariant lattice features and richer pore/connectivity descriptors.

D. LLM Fine-Tuning: Prompt Ablation with CIF-derived Metadata

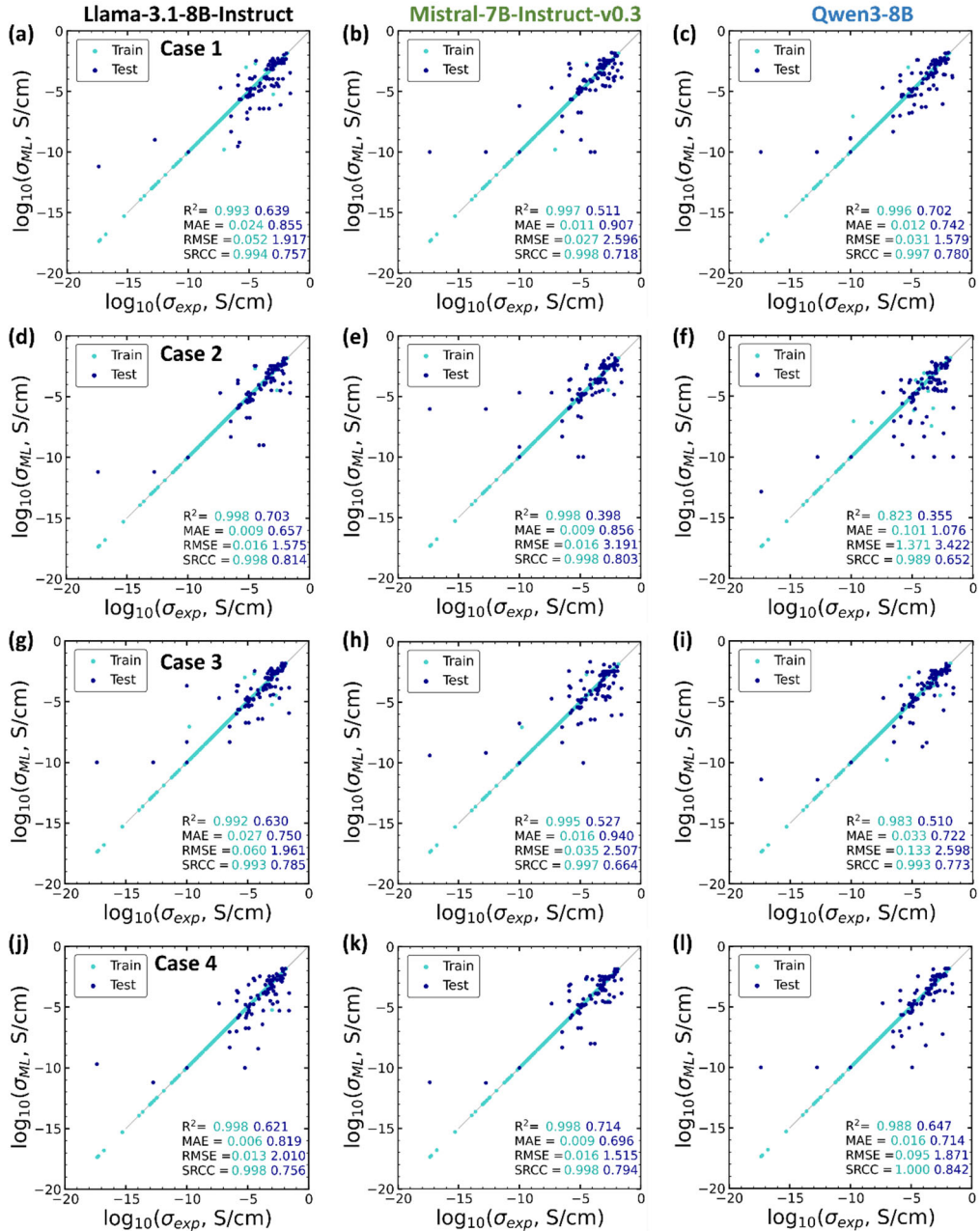


Figure 8. (a)-(c) The results for Case 1. (d)-(f) The results for Case 2. (g)-(i) The results for Case 3. (j)-(l) The results for Case 4.

Having established the importance of structural features using GBR, we next evaluated whether Large Language Models could capture these structure-property relationships directly from textural descriptors, thereby bypassing the need for explicit geometric feature engineering.

Figure 8 illustrates the prediction results for the train and test sets across four different cases of three Large Language Models (LLMs): Llama-3.1-8B-Instruct, Mistral-7B-Instruct-v0.3, and Qwen3-8B. The performance is evaluated by plotting the logarithm of LLM-predicted conductivity against the logarithm of the experimental ionic conductivity at room temperature. For evaluation metrics, R^2 , MAE, RMSE and SRCC are used to quantify predictive accuracy for test set. Among the three models, Llama-3.1-8B-Instruct demonstrates consistently strong predictive performance, particularly in Case 2 (**Figure 8(d)**). In this case, which incorporates compositional features and symmetry information, the model achieves the lowest MAE of 0.657 and the highest SRCC of 0.814 across all models and feature cases. Mistral-7B-Instruct-v0.3 achieves its best performance in Case 4 (**Figure 8(k)**), where all available features which include compositional information, symmetry group, and disorder descriptors are included. In this setting, it records the lowest RMSE of 1.515 and the highest R^2 of 0.714 among all evaluated configurations. In contrast, the predictive performance of both models degrades in Case 1 (**Figure 8(a,b)**), which relies solely on chemical formula features, and in Case 3 (**Figure 8(g,h)**), which combines formula features with disorder descriptors but excludes symmetry information. The Qwen3-8B model performs best in Case 4 (**Figure 8(l)**), where the full set of compositional and structural descriptors is used. Conversely, its weakest performance is observed in Case 2 (**Figure 8(f)**), which includes compositional features and symmetry information but omits disorder descriptors. LLMs can achieve competitive room-temperature conductivity prediction from compact text descriptors, with the best case requiring not only the chemical formula and structural descriptors. Importantly, incorporating symmetry and disorder metadata generally improves predictive performance, although the magnitude of the benefit is

model-dependent. This suggests that the effectiveness of such metadata depends on how prompt content interacts with each model’s pretraining and fine-tuning dynamics.

E. Cross-Model Comparison and Applicability

To place our results in context, **Table 7** compares our room-temperature (RT) models with previously published models trained on experimental conductivity datasets. Because several prior studies were trained on datasets spanning broad temperature ranges (e.g., 5 – 873 °C), their reported MAEs are not strictly comparable to RT-only evaluations; we therefore include them as a qualitative reference point rather than a direct benchmark. On our curated RT dataset ($n = 499$), the fine-tuned LLM case (Llama-3.1-8B-Instruct, Case 2:formula and symmetry) achieves $MAE = 0.657$ in $\log_{10}(\sigma / (\text{S} \cdot \text{cm}^{-1}))$, while the best GBR model achieves $MAE = 0.543$. In \log_{10} units, an MAE of 0.543 corresponds to an average multiplicative uncertainty of $\sim 3.4x$ in conductivity. Relative to prior experimental-data-driven models, our controlled RT evaluation highlights the trade-off between interpretability (GBR+SHAP) and minimal feature engineering (LLM), while noting that direct MAE comparisons across studies are limited by different temperature ranges and dataset composition.

Table 7. Test Set MAE (in $\log_{10}(\sigma / (\text{S} \cdot \text{cm}^{-1}))$) for experimental-data-driven ionic conductivity prediction. Prior studies span different temperature ranges; RT-only vs. multiple-temperature results are included for context and are not strictly directly comparable.

Models	Features	# of Data	Test MAE ($\log_{10}(\sigma / (\text{S} \cdot \text{cm}^{-1}))$)	Reference
CrabNet	Composition (5 - 873 °C)	820	0.85	[15]
CatBoost	Composition (5 - 873 °C)	895	0.831	[17]
RF	Composition, RT	599	1.54	[20]
p-CGCNN	Structure, RT	321	2.52	[20]
GBR	Composition, Structure, RT	499	0.543	-
LLM (Llama-3.1-8B-Instruct)	Text prompt (formula, symmetry), RT	499	0.657	-

Because the target is \log_{10} conductivity, a difference of 0.02 – 0.03 MAE corresponds to a modest change in the typical multiplicative error factor; therefore, interpretability (GBR plus

SHAP) and representation convenience (LLM prompts) become key practical differentiators. To assess model performance across different families, test set MAE values were compared by category as shown in **Table 8**. Among sulfide electrolytes, argyrodite structures containing halide anions exhibit distinct conductivity ranges compared to conventional non-halide sulfides and oxides⁶². Therefore, we classified the solid electrolytes into oxides, non-halide sulfides, halides, and others, and compared the prediction performance for each category. Family-resolved errors show that both models are most reliable where training coverage is dense (oxides/sulfides) and degrade for underrepresented chemistries, emphasizing dataset coverage, not just architecture, as the key limitation for generalization.

Table 8. Model performance on ionic conductivity prediction by electrolyte family.

Family	Types	# of Structures in Test Set	GBR Test MAE ($\log_{10}(\sigma/\text{S cm}^{-1})$)	LLM Test MAE ($\log_{10}(\sigma/\text{S cm}^{-1})$)
Oxide	Garnet (LLZO), NASICON (LATP), Perovskite (LLTO)	57	0.503	0.629
Sulfide (non-halides)	LGPS, thio-phosphate	11	0.245	0.654
Sulfide (halides)	Argyrodite ($\text{Li}_6\text{PS}_5\text{X}$, X = Cl, Br, I)	27	0.501	0.380
Others (non-S /O)*	Thio-LISICON derivatives halides phosphates	5	1.874	1.781

*Limited sample size (n=5); results should be interpreted with caution.

Table 8 shows that oxides and sulfides, which are well represented in the dataset, were predicted with high accuracy. In contrast, derivatives such as thio-LISICON compounds (e.g., Li_4SnSe_4), halides (e.g., Li_2VCl_4), and phosphates (e.g., Li_8GeP_4) showed the lowest accuracy, with average MAEs of 1.874 for GBR and 1.781 for LLM. Although both models exhibited the lowest performance for these compounds, the prediction error of the GBR model was higher than LLM model. However, in the case of non-halide sulfides, the MAE of the LLM model

was 0.654, which was more than twice as high as that of the GBR model. In addition to MAE, both models show strong rank-ordering capability (SRCC), indicating the usefulness of the developed model when integrated into a computational screening workflow.

Predicted ionic conductivities for representative high-performance electrolytes were compared with experimental measurements in **Table 9**. For well-studied structures, predictions closely match experimentally reported values, which we attribute to the large number of compositionally and structurally similar cases in the training data. By contrast, accuracy decreased for uncommon structures deviating from the conventional oxide and sulfide families, where relevant training sets are limited. For the LLM, we observe that structures with compositions similar to those in the training set were often assigned to ionic conductivity values identical to the training labels. This indicates limited extrapolation and low output diversity for unseen numeric ranges in the text-based setting. The GBR model shows sensitivity to the width of feature coverage in the training data. These findings suggest that expanding the experimental dataset to cover a wider range of elements and stoichiometries is essential for improving the generalization of both models. Representative predictions illustrate that canonical families are predicted accurately, whereas uncommon chemistries expose extrapolation limits, particularly for text-based models that may default toward familiar label ranges when prompts resemble training examples.

Table 9. Predicted ionic conductivities of representative solid electrolytes from each family compared with experimental values.

Family	Composition	Exp. $\log_{10}(\sigma/\text{S cm}^{-1})$	GBR $\log_{10}(\sigma/\text{S cm}^{-1})$	LLM $\log_{10}(\sigma/\text{S cm}^{-1})$
Oxide	$\text{Li}_7\text{La}_3\text{Zr}_2\text{O}_{12}$	-4.638	-4.258	-5.710
	$\text{Li}_6\text{BaLa}_2\text{Ta}_2\text{O}_{12}$	-4.886	-4.833	-5.270
Sulfide (non- halides)	$\text{Li}_{10}\text{GeP}_2\text{S}_{12}$	-1.917	-1.962	-1.850
	$\text{Li}_{10}\text{Ge}_{0.66}\text{Sn}_{0.33}\text{P}_2\text{S}_{12}$	-2.194	-1.747	-2.320

Sulfide (halides)	Li ₆ PS ₅ Br	−3.154	−3.526	−4.490
	Li ₆ PS ₅ I	−5.900	−3.929	−3.920
Others (non- S /O)	Li ₈ GeP ₄	−4.066	−4.464	−5.240
	Li ₄ SnSe ₄	−4.699	−6.715	−4.700

IV. Conclusion

In this work, we successfully developed machine learning models for predicting the ionic conductivity of solid-state electrolytes by integrating both composition- and structure-based features. A total of 499 CIF structures were compiled, including 152 structures generated via a genetic algorithm using USPEX. The best-performing GBR model demonstrated that combining stoichiometric and geometric features significantly improved predictive accuracy, achieving a test R^2 of 0.840 and a test MAE of 0.543 log(S/cm), compared to models trained with only one feature type. SHAP analysis further revealed that both compositional and structural properties contribute substantially to model performance, with lattice parameter b , the S/O ratio, density (g/cm³) and POAV (cm³/g) identified as key descriptors. We introduced a text-based approach based on a fine-tuning several large language models (LLMs) using text representations of compositional and structural features. This method eliminated the need for geometry optimization while maintaining high predictive accuracy, with MAE of 0.657 log(S/cm). Comparison with previously reported experimental-data-based models confirmed that our framework achieves superior accuracy despite the limited size of the available dataset.

Overall, our results demonstrate that incorporating structural information into both GBR and LLM models enhances the predictive capability for ionic conductivity. However, the limited range of experimentally measured ionic conductivities currently available constrains a rigorous evaluation of model extrapolation to novel materials. A key limitation of our framework is its reduced extrapolation capability for materials that fall outside the compositional and structural

domain of the training set. Because the dataset primarily consists of dense oxide- and sulfide-based solid electrolytes, the model may underperform for systems with highly porous frameworks or well-defined ion-channel geometries whose pore volumes, densities, or channel topologies deviate from those represented in the training structures. Additionally, our computational framework does not explicitly account for the potential energy landscape governing ion migration or the ion–ion correlation effects that can arise at high carrier concentrations. Recent developments in interaction-aware neural potentials, such as the methodology proposed by Gustafsson et al⁶³, demonstrate that capturing many body ion–ion correlations and mapping energy landscapes can provide deeper mechanistic insight into solid-state ionic transport. Incorporating such energy-landscape-based or interaction-aware descriptors lies beyond the scope of the present work but represents an important direction for future development. While the ML work developed here is focused on providing structure–property correlations using global crystal and compositional features, incorporating electrostatic landscape information for ion transport represents an important direction for future studies to provide deeper chemical and material insight for next-generation solid-state electrolyte design and discovery.

Supplementary material

ACKNOWLEDGMENTS

This work was supported by the National Research Foundation of Korea (NRF) from a grant funded by the Korea government (MSIT) (RS-2024-00449431). The computational resources were provided by KISTI (KSC-2024-CRE-0412). This research was supported by the Regional Innovation System & Education (RISE) program through the Institute of Regional Innovation System & Education in Busan Metropolitan City, funded by the Ministry of Education (MOE) and Busan Metropolitan City, Republic of Korea (2025-RISE-02-001-020).

AUTHOR DECLARATIONS

Conflict of Interest

The authors have no conflicts to disclose.

Author Contributions

Haewon Kim: Data curation; Software; Formal analysis; Investigation; Methodology; Validation; Visualization; Writing – original draft; Writing – review & editing. **Taekgi Lee:** Investigation; Software; Methodology; Validation; Visualization; Writing – original draft; Writing – review & editing. **Seong Eun Hong:** Data curation; Methodology; Investigation. **Kyeong-Ho Kim:** Writing – review & editing. **Yongchul G. Chung:** Conceptualization; Formal analysis; Resources; Supervision; Project administration; Funding acquisition; Writing – review & editing.

DATA AVAILABILITY

Developed machine learning models and structure generation data are available on <https://github.com/Chung-Research-Group/reproducible-workflows/tree/master/2025-SSE>, the dataset can be accessed from <https://doi.org/10.5281/zenodo.17157647>.

REFERENCES

1. J. G. Kim, B. Son, S. Mukherjee, N. Schuppert, A. Bates, O. Kwon, M. J. Choi, H. Y. Chung and S. Park, *J. Power Sources* 282, 299–322 (2015).
<https://doi.org/10.1016/j.jpowsour.2015.02.054>
2. A. Chen, C. Qu, Y. Shi, and F. Shi, *Front. Energy Res.* Volume 8 (2020).
<https://doi.org/10.3389/fenrg.2020.571440>
3. K. Kerman, A. Luntz, V. Viswanathan, Y.-M. Chiang, and Z. Chen, *J. Electrochem. Soc.* 164, A1731 (2017). <https://doi.org/10.1149/2.1571707jes>
4. F. Han, T. Gao, Y. Zhu, K. J. Gaskell, and C. Wang, *Adv. Mater.* 27, 3473–3483 (2015).
<https://doi.org/10.1002/adma.201500180>
5. Z. Zhang, Y. Shao, B. Lotsch, Y.-S. Hu, H. Li, J. Janek, L. F. Nazar, C.-W. Nan, J. Maier, M. Armand, and L. Chen, *Energy Environ. Sci.* 11, 1945–1976 (2018).
<https://doi.org/10.1039/C8EE01053F>
6. A. L. Davis, V. Goel, D. W. Liao, M. N. Main, E. Kazyak, J. Lee, K. Thornton and N. P., *ACS Energy Lett.* 6, 2993–3003 (2021). <https://doi.org/10.1021/acsenergylett.1c01063>
7. R. Zwanzig, *Annu. Rev. Phys. Chem.* 16, 67–102 (1965).
<https://doi.org/10.1146/annurev.pc.16.100165.000435>
8. Z. Zhu and Y. Zhu, *Acc. Mater. Res.* 3, 1101–1105 (2022).
<https://doi.org/10.1021/accountsmr.2c00184>
9. B. Deng, Y. Choi, P. Zhong, J. Riebesell, S. Anand, Z. Li, K. Jun, K. A. Persson and G. Ceder, *npj Comput. Mater.* 11, 9 (2025). <https://doi.org/10.1038/s41524-024-01500-6>
10. M. French, S. Hamel, and R. Redmer, *Phys. Rev. Lett.* 107, 185901 (2011).
<https://doi.org/10.1103/PhysRevLett.107.185901>
11. R. Sasaki, B. Gao, T. Hitosugi, and Y. Tateyama, *npj Comput. Mater.* 9, 48 (2023).
<https://doi.org/10.1038/s41524-023-00996-8>

12. Z. Xu, H. Duan, Z. Dou, M. Zheng, Y. Lin, Y. Xia, H. Zhao, and Y. Xia, *npj Comput. Mater.* 9, 105 (2023). <https://doi.org/10.1038/s41524-023-01049-w>
13. R. Wang, M. Guo, Y. Gao, X. Wang, Y. Zhang, B. Deng, M. Shi, L. Zhang and Z. Zhong, *npj Comput. Mater.* 11, 266 (2025). <https://doi.org/10.1038/s41524-025-01764-6>
14. S. C. Selvaraj, V. Koverga, and A. T. Ngo, *J. Electrochem. Soc.* 171, 050544 (2024). <https://doi.org/10.1149/1945-7111/ad4ac9>
15. C. J. Hargreaves, M. W. Gaulois, L. M. Daniels, E. J. Watts, V. A. Kurlin, M. Moran, Y. Dang, R. Morris, A. Morscher, K. Thompson, M. A. Wright, B.-E. Prasad, F. Blanc, C. M. Collins, C. A. Crawford, B. B. Duff, J. Evans, J. Gamon, G. Han, B. T. Leube, H. Niu, A. J. Perez, A. Robinson, O. Rogan, P. M. Sharp, E. Shoko, M. Sonni, W. J. Thomas, A. Vasylenko, L. Wang, M. J. Rosseinsky and M. S. Dyer, *npj Comput. Mater.* 9, 9 (2023). <https://doi.org/10.1038/s41524-022-00951-z>
16. A. Y.-T. Wang, S. K. Kauwe, R. J. Murdock, and T. D. Sparks, *npj Comput. Mater.* 7, 77 (2021). <https://doi.org/10.1038/s41524-021-00545-1>
17. J. Yu, L. Jin, Y. Ji, and Y. Li, *Mater. Chem. Front.* (2025). <https://doi.org/10.1039/d5qm00438a>
18. Y. Zhang, X. He, Z. Chen, Q. Bai, A. M. Nolan, C. A. Roberts, D. Banerjee, T. Matsunaga, Y. Mo, and C. Ling, *Nat. Commun.* 10, 5260 (2019). <https://doi.org/10.1038/s41467-019-13214-1>
19. L. Prokhorenkova, G. Gusev, A. Vorobev, A. V. Dorogush, and A. Gulin, *Adv. Neural Inf. Process. Syst.* 31 (2018). <https://doi.org/10.48550/arXiv.1706.09516>
20. J. A. H. Félix Therrien, D. Sharma, R. Hendley, A. Hernández-García, S. Sun, A. Tchagang, J. Su, S. Huberman, Y. Bengio, H. Guo, and H. Shin, *arXiv* 2502.14234 (2025). <https://doi.org/10.48550/arXiv.2502.14234>

21. F. A. L. Laskowski, D. B. McHaffie, and K. A. See, *Energy Environ. Sci.* 16, 1264–1276 (2023). <https://doi.org/10.1039/D2EE03499A>
22. E. van der Maas, T. Famprakis, S. Pieters, J. P. Dijkstra, Z. Li, S. R. Parnell, R. I. Smith, E. R. H. van Eck, S. Ganapathy, and M. Wagemaker, *J. Mater. Chem. A* 11, 4559–4571 (2023). <https://doi.org/10.1039/D2TA08433C>
23. D. B. McHaffie, Z. W. B. Iton, J. M. Bienz, F. A. L. Laskowski and K. A. See, *Digit. Discov.* 4, 1518–1533 (2025). <https://doi.org/10.1039/D5DD00052A>
24. S. Ito, K. Muraoka, and A. Nakayama, *Chem. Mater.* 37, 2447–2456 (2025). <https://doi.org/10.1021/acs.chemmater.4c02726>
25. Y. Kang and J. Kim, *Nat. Commun.* 15, 4705 (2024). <https://doi.org/10.1038/s41467-024-48998-4>
26. J. Lu, Z. Song, Q. Zhao, Y. Du, Y. Cao, H. Jia and C. Duan, *J. Am. Chem. Soc.* 147 (36), 32377-32388 (2025). <https://pubs.acs.org/doi/full/10.1021/jacs.5c02097>
27. H. Zhou, F. Liu, J. Wu, W. Zhang, G. Huang, L. Clifton, D. Eyre, H. Luo, F. Liu, K. Branson, P. Schwab, X. Wu, Y. Zheng, A. Thakur and D. A. Clifton, *Nat. Biomed. Eng.* (2025). <https://doi.org/10.1038/s41551-025-01471-z>
28. C. Akshat, G. Chakradhar, H. Hongshuo, and F. Amir Barati, *Comput. Mater. Sci.* 244, 113256 (2024). <https://doi.org/10.1016/j.commatsci.2024.113256>
29. S. Kamnis and K. Delibasis, *Sci. Rep.* 15, 11861 (2025). <https://doi.org/10.1038/s41598-025-95170-z>
30. S. Agarwal, A. Mahmood, and R. Ramprasad, *ACS Mater. Lett.* 7, 2017–2023 (2025). <https://doi.org/10.1021/acsmaterialslett.5c00054>
31. A. Niyongabo Rubungo, C. Arnold, B. P. Rand, and A. B. Dieng, *npj Comput. Mater.* 11, 186 (2025). <https://doi.org/10.1038/s41524-025-01536-2>

32. A. M. Ganose and A. Jain, *MRS Commun.* 9, 874–881 (2019).
<https://doi.org/10.1557/mrc.2019.94>

33. A. O. Lyakhov, A. R. Oganov, H. T. Stokes, and Q. Zhu, *Comput. Phys. Commun.* 184, 1172–1182 (2013). <https://doi.org/10.1016/j.cpc.2012.12.009>

34. A. R. Oganov and C. W. Glass, *J. Chem. Phys.* 124, 244704 (2006).
<https://doi.org/10.1063/1.2210932>

35. A. R. Oganov, A. O. Lyakhov, and M. Valle, *Acc. Chem. Res.* 44, 227–237 (2011).
<https://doi.org/10.1021/ar1001318>

36. A. Oganov, Y. ma, C. Glass and M. Valle, *Psi-k Newslett.* 84 (2007).

37. A. P. Thompson, H. M. Aktulga, R. Berger, D. S. Bolintineanu, W. M. Brown, P. S. Crozier, P. J. in 't Veld, A. Kohlmeyer, S. G. Moore, T. D. Nguyen, R. Shan, M. J. Stevens, J. Tranchida, C. Trott and S. J. Plimpton, *Comput. Phys. Commun.* 271, 108171 (2022). <https://doi.org/10.1016/j.cpc.2021.108171>

38. B. Deng, P. Zhong, K. Jun, J. Riebesell, K. Han, C. J. Bartel, and G. Ceder, *Nat. Mach. Intell.* 5, 1031–1041 (2023). <https://doi.org/10.1038/s42256-023-00716-3>

39. H. Yu, M. Giantomassi, G. Materzanini, J. Wang, and G.-M. Rignanese, *Mater. Genome Eng. Adv.* 2, e58 (2024). <https://doi.org/10.1002/mgea.58>

40. G. Boyer, *GitHub* (2024). <https://github.com/gmboyer/chemparse>

41. D. Ongari, P. G. Boyd, S. Barthel, M. Witman, M. Haranczyk, and B. Smit, *Langmuir* 33, 14529–14538 (2017). <https://doi.org/10.1021/acs.langmuir.7b01682>

42. M. Pinheiro, R. L. Martin, C. H. Rycroft, and M. Haranczyk, *CrystEngComm* 15, 7531–7538 (2013). <https://doi.org/10.1039/C3CE41057A>

43. T. F. Willems, C. H. Rycroft, M. Kazi, J. C. Meza, and M. Haranczyk, *Microporous Mesoporous Mater.* 149, 134–141 (2012).
<https://doi.org/10.1016/j.micromeso.2011.08.020>

44. M. K. Tufail, P. Zhai, M. Jia, N. Zhao, and X. Guo, *Energy Mater. Adv.* 4, 0015 (2023).
<https://doi.org/10.34133/energymatadv.0015>

45. H. Yang and N. Wu, *Energy Sci. Eng.* 10, 1643–1671 (2022).
<https://doi.org/10.1002/ese3.1163>

46. Y. Wang, W. D. Richards, S. P. Ong, L. J. Miara, J. C. Kim, Y. Mo, and G. Ceder, *Nat. Mater.* 14, 1026–1031 (2015). <https://doi.org/10.1038/nmat4369>

47. M. S. Diallo, T. Shi, Y. Zhang, X. Peng, I. Shozib, Y. Wang, L. J. Miara, M. C. Scott, Q. H. Tu, and G. Ceder, *Nat. Commun.* 15, 858 (2024). <https://doi.org/10.1038/s41467-024-45030-7>

48. F. Pedregosa, G. Varoquaux, A. Gramfort, V. Michel, B. Thirion, O. Grisel, M. Blondel, P. Prettenhofer, R. Weiss, and V. Dubourg, *J. Mach. Learn. Res.* 12, 2825–2830 (2011).
<https://dl.acm.org/doi/10.5555/1953048.2078195>

49. J. Howard and S. Ruder, *arXiv* 1801.06146 (2018).
<https://doi.org/10.48550/arXiv.1801.06146>

50. T. Wolf, L. Debut, V. Sanh, J. Chaumond, C. Delangue, A. Moi, ... and A. M. Rush, *arXiv* 1910.03771 (2019). <https://doi.org/10.48550/arXiv.1910.03771>

51. D. H. and M. Han, *GitHub* (2023). <https://github.com/unslothai/unsloth>

52. E. J. Hu, Y. Shen, P. Wallis, Z. Allen-Zhu, Y. Li, S. Wang, ... and W. Chen, *ICLR* 1, 3 (2022). <https://doi.org/10.48550/arXiv.2106.09685>

53. A. N. Rubungo, K. Li, J. Hattrick-Simpers, and A. B. Dieng, *Mach. Learn.: Sci. Technol.* 6, 020501 (2025). <https://doi.org/10.1088/2632-2153/add3bb>

54. M. Botros and J. Janek, *Science* 378, 1273–1274 (2022).
<https://doi.org/10.1126/science.adf3383>

55. P. Zhong, S. Gupta, B. Deng, K. Jun, and G. Ceder, *ACS Energy Lett.* 9, 2775–2781 (2024). <https://doi.org/10.1021/acsenergylett.4c00799>

56. S. K. Choi, J. Han, G. J. Kim, Y. H. Kim, J. Choi, and M. Yang, *J. Powder Mater.* 31, 293–301 (2024). <https://doi.org/10.4150/jpm.2024.00206>

57. H. Fang and P. Jena, *Proc. Natl. Acad. Sci. U.S.A.* 114, 11046–11051 (2017). <https://doi.org/10.1073/pnas.1704086114>

58. J. Riebesell, R. Goodall, and S. Baird, *GitHub* (2022). <https://github.com/janosh/pymatviz>

59. L. Gao, X. Zhang, J. Zhu, S. Han, H. Zhang, L. Wang, R. Zhao, S. Gao, S. Li, Y. Wang, D. Huang, Y. Zhao, and R. Zou, *Nat. Commun.* 14, 6807 (2023). <https://doi.org/10.1038/s41467-023-42385-1>

60. N.J.J. de Klerk, E. van der Maas, and M. Wagemaker, *ACS Appl Energy Mater* 1, 3230–3242 (2018). <https://pubs.acs.org/doi/10.1021/acsaem.8b00457>

61. M. Umair, S. Zhou, W. Li, H. T. H. Rana, J. Yang, L. Cheng, M. Li, S. Yu, and J. Wei, *Batter. Supercaps* 8, e202400667 (2025). <https://doi.org/10.1002/batt.202400667>

62. H. Kwak, S. Wang, J. Park, Y. Liu, K. T. Kim, Y. Choi, Y. Mo, and Y. S. Jung, *ACS Energy Lett.* 7, 1776–1805 (2022). <https://doi.org/10.1021/acsenergylett.2c00438>

63. H. Gustafsson, M. Kozdra, B. Smit, S. Barthel and A. Mace, *J. Chem. Theory Comput.* 20 (1), 18-29 (2024). <https://pubs.acs.org/doi/10.1021/acs.jctc.3c01005>